

Boundary Discretization and Reliable Classification Network for Temporal Action Detection

Zhenying Fang

Abstract—Temporal action detection aims to recognize the action category and determine the starting and ending time of each action instance in untrimmed videos. The mixed methods have achieved remarkable performance by seamlessly merging anchor-based and anchor-free approaches. Nonetheless, there are still two crucial issues within the mixed framework: (1) Brute-force merging and handcrafted anchors design hinder the substantial potential and practicality of the mixed methods. (2) Within-category predictions show a significant abundance of false positives. In this paper, we propose a novel Boundary Discretization and Reliable Classification Network (BDRC-Net) that addresses the aforementioned issues by introducing boundary discretization and reliable classification modules. Specifically, the boundary discretization module (BDM) elegantly merges anchor-based and anchor-free approaches in the form of boundary discretization, eliminating the need for the traditional handcrafted anchor design. Furthermore, the reliable classification module (RCM) predicts reliable global action categories to reduce false positives. Extensive experiments conducted on different benchmarks demonstrate that our proposed method achieves favorable performance compared with the state-of-the-art at high temporal intersection over union (tIoU) thresholds. For example, on the THUMOS'14 dataset, BDRC-Net surpasses the previous best $mAP@tIoU = 0.9$ by 2.8% and 1.4% when utilizing the ActionFormer and TriDet backbones, respectively. Our source code is available at <https://github.com/zhenyingfang/BDRC-Net>.

Index Terms—Temporal action detection, boundary discretization, reliable classification.

I. INTRODUCTION

TEMPORAL Action Detection (TAD) is a fundamental yet challenging task of video understanding, aiming to identify and localize action instances within untrimmed videos. Various applications, such as video summarization [1], intelligent surveillance [2], and human behavior analysis [3], [4], can be feasible with the help of TAD.

The TAD methods can be classified into three types: anchor-based, anchor-free, and mixed. Anchor-based methods [5]–[9] rely on the manually defined anchors, and their performance is sensitive to the number and scale of anchors designed. Thanks to the assistance of carefully designed anchors, their prediction stability is better. Anchor-free methods [10]–[14] densely predict action categories and corresponding boundaries on every snippet of the entire video. Compared with anchor-based methods, they can detect more flexible continuous actions. Recently, mixed methods [15]–[17] achieving remarkable results by combining the two methods mentioned above. While maintaining the stability of the anchor-based methods,

TABLE I
REMOVING FALSE POSITIVE CATEGORY PREDICTIONS IMPROVES THE PERFORMANCE ON THUMOS'14 OF MIXED METHOD A2NET AND ANCHOR-FREE METHOD ACTIONFORMER. †: OUR REPRODUCE.

Method	mAP@tIoU(%)						
	0.1	0.2	0.3	0.4	0.5	0.6	0.7
A2Net [†]	67.9	65.6	61.8	54.3	44.5	33.0	19.1
A2Net_remove_fp [†]	73.4 († 5.5)	70.8 († 5.2)	66.7 († 4.9)	58.3 († 4.0)	47.2 († 2.7)	34.5 († 1.5)	19.8 († 0.7)
ActionFormer	85.4	84.5	82.1	77.8	71.0	59.4	43.9
ActionFormer_remove_fp	87.8 († 2.4)	86.9 († 2.4)	84.6 († 2.5)	80.0 († 2.2)	73.0 († 2.0)	61.4 († 2.0)	45.6 († 1.7)

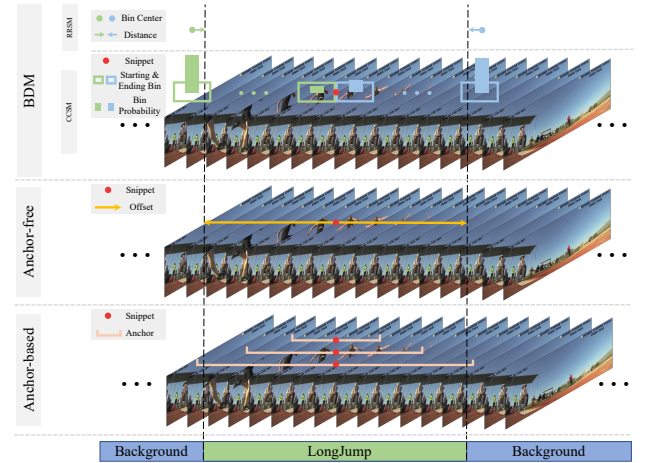


Fig. 1. Comparison of boundary discretization, anchor-based, and anchor-free methods for representing action boundaries.

flexibility has been enhanced by relying on the anchor-free methods.

Despite achieving remarkable detection performance, mixed methods still suffer from two crucial issues: (1) Brute-force merging and handcrafted anchors design affect the performance and practical application of the mixed methods. Existing mixed methods predict action instances with anchor-based and anchor-free branches, respectively, and directly merge these results through post-processing to obtain mixed results. This merging method, through post-processing, increases computational complexity while reducing inference speed. Meanwhile, the anchor-based branch requires carefully handcrafted designed anchors to achieve optimal performance on different datasets, which is not conducive to the practical application of TAD. (2) The detection results of existing TAD methods contain a large number of false positive category predictions, which further impact the detection performance. Predicting action categories for each snippet of the entire video in the anchor-free branch creates a large number of false positives due to the impact of non-discriminative snippets. As

Z. Fang is with the School of Computer and Information Engineering, Hefei University of Technology, China, 188065. Email: zhenyingfang@mail.hfut.edu.cn.

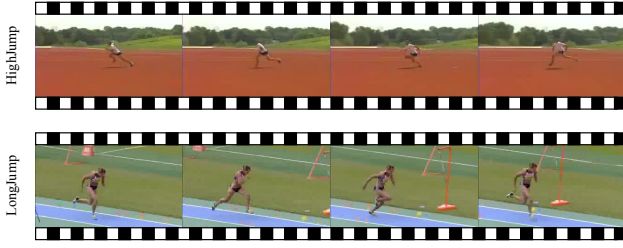


Fig. 2. Example of non-discriminative snippets. It is impossible to accurately classify them with only partial snippets from two action categories, namely *HighJump* and *LongJump*.

shown in Table I, when filtering out false positives from both the mixed method A2Net [17] and the anchor-free method ActionFormer [14], their performance is greatly improved at all tIoU thresholds.

To address the abovementioned issues, we propose a novel framework called BDRC-Net, consisting of a boundary discretization module (BDM) and a reliable classification module (RCM).

(1) As shown in Fig. 1, BDM represents action boundaries using two sub-modules: coarse classification and refined regression. The coarse classification sub-module (CCSM) discretizes the boundary offsets corresponding to each snippet into multiple bins and predicts which bin the starting and ending boundaries belong to. As each discretized bin encompasses multiple positions, we opt to utilize the central position of each bin as its corresponding location prediction to generate coarse results. Then, the refined regression sub-module (RRSM) enhances the CCSM by regressing the distance between the coarse results and the actual action boundaries. In BDM, the discretized bins can be regarded as pseudo anchors, which preserve the benefit of anchor-based methods in terms of stability. At the same time, the RRSM improves the flexibility of boundary predictions by distance regression. The two sub-modules are elegantly combined by sharing features, avoiding the reliance on carefully designed anchors and addressing the highly computational cost issue of existing mixed methods.

(2) Only discriminative snippets are easily recognized in a complete action, while non-discriminative snippets are similar to the background or other action categories. In Fig. 2, we illustrate the non-discriminative snippets among action instances of different action categories. These non-discriminative snippets have similar motion information, making distinguishing the actual action categories difficult. Anchor-free methods classify the action categories to which each snippet belongs in the entire video, and non-discriminative snippets are prone to classification errors, resulting in false positives. To this end, RCM predicts reliable categories to filter out false positives. Following the design of weakly supervised temporal action detection [18]–[20], we employ Multiple Instance Learning (MIL) to predict reliable video-level action categories. Specifically, for each action category, RCM selects highly scored discriminative snippets and aggregates their prediction probabilities to obtain reliable video-level probability. These video-level probabilities are used to filter snippet-level predictions.

Extensive experiments on THUMOS’14 and ActivityNet-

1.3 demonstrate that our method surpasses the state-of-the-art. Furthermore, the ablation studies validate the effectiveness of each component in BDRC-Net.

In summary, the contributions of this paper are as follows:

- We propose an elegant mixed-method boundary discretization module (BDM). BDM predicts action boundaries through a coarse classification sub-module (CCSM) and a refined regression sub-module (RRSM). CCSM discretizes boundary offsets into multiple bins and predicts which bin the action boundaries belong to, resulting in coarse results. RRSM refines the coarse results by regressing the distance between the coarse results and the actual action boundaries.
- We propose a reliable classification module (RCM) for predicting reliable action categories. RCM predicts the action categories occurring in the entire video by aggregating highly discriminative snippets, making its results more reliable than predicting the categories for each snippet individually. It is used to filter out false positives in snippet-level predictions.
- Extensive experimental results demonstrate that our method surpasses the state-of-the-art.

II. RELATED WORK

In this section, we review the previous works related to our paper, which are divided into three parts: (1) anchor-based TAD, (2) anchor-free TAD, and (3) mixed TAD.

A. Anchor-based TAD

Anchor-based methods [5]–[9], [21]–[23] classify each pre-defined anchor obtained from the distribution of action instances in the dataset while also regressing their action boundaries; it can be classified into *one-stage methods* [5], [21] and *two-stage methods* [6]–[9], [22], [23]. One-stage methods predict boundaries for all anchors. SSAD [5], an early one-stage TAD method, uses multi-scale features to predict each anchor’s category, overlap, and regression offset. Later, Decouple-SSAD [21] reduces the mutual influence between the classification and regression branches during multi-task training by decoupling them. Two-stage methods generate action proposals using pre-defined anchors and subsequently classify and perform regression on these proposals. R-C3D [6] was the first to propose an end-to-end trained two-stage method, and its architecture served as the main inspiration for Faster R-CNN [24]. TBOS [8] enhances the feature representation for the TAD task by utilizing multi-task learning. More recently TallFormer [9] uses a long-term memory mechanism to capture video information and enable end-to-end training. Anchor-based methods usually set multiple anchors at each position, which implements a dense coverage for action instances, and enhances the stability of the predictions.

B. Anchor-free TAD

The anchor-based methods depend on the pre-definition of anchors for various datasets, which restricts their flexibility in terms of detection and application. Anchor-free methods

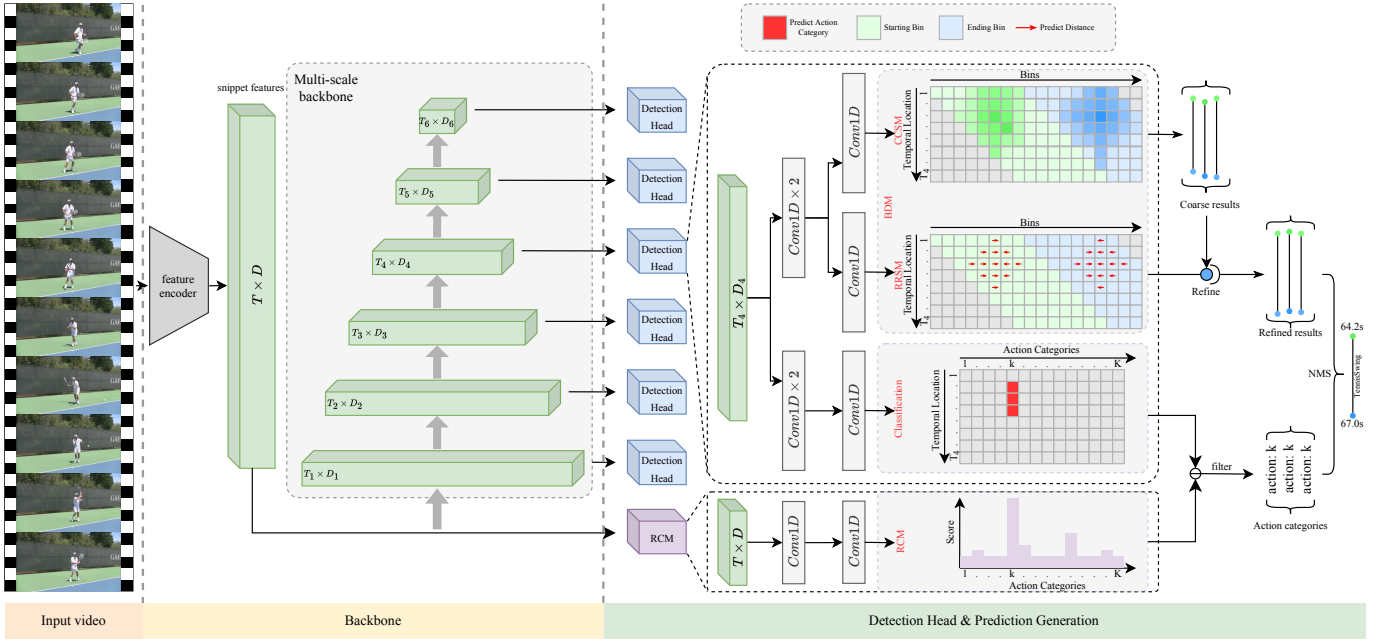


Fig. 3. **Architecture Overview.** Given an untrimmed video, the feature encoder extracts snippet features. Then, the multi-scale backbone (MSB) is used to extract multi-scale spatio-temporal features. Finally, the BDM in the detection head predicts action boundaries on each snippet, and the classification module is used to predict the action categories for each snippet. Specifically, our RCM predicts the video-level action categories based on snippet features, which are used to filter out false positives in the classification module.

[10]–[14], [25], on the other hand, do not rely on pre-defined anchors, resulting in more flexible and versatile predictions. SSN [10] first introduces the concept of actionness, which uses actionness to generate proposals and then performs two-stage predictions. RAM [26] introduces relation attention to exploiting informative relations among proposals, further improving the performance of SSN. Subsequently, BSN [11] divides action boundaries into starting and ending intervals and performs localization by predicting boundary probabilities. AFSD [12] designs a saliency-based refinement module to refine the boundaries of the anchor-free method. Recently, ActionFormer [14] utilizes local self-attention to extract features from videos and introduces a multi-scale transformer block to predict action instances. EAC [27] explicitly modeling action centers to reduce unreliable action detection results caused by ambiguous action boundaries.

C. Mixed TAD

Mixed TAD attempts to merge the advantages of the two methods above to achieve more stable and precise detection results with better boundaries. PCAD [15] explores enhancing the prediction flexibility by directly merging the boundary probabilities in a two-stage anchor-based method. MGG [16] also explores the fusion of anchor-based and boundary probabilities. Unlike PCAD, MGG utilizes the starting and ending probabilities to refine the boundaries of the anchor-based. Recently, A2Net [17] conducted a comprehensive comparison between the anchor-based and anchor-free methods, verifying their complementary. When inferencing, A2Net combines the results from the two methods and employs non-maximum suppression [28] to suppress redundant predictions.

The existing mixed methods violently merge anchor-based and anchor-free methods and depend on handcrafted anchors design. It limits the mixed method’s performance and affects the practical application of TAD. Moreover, the false positives in snippet-level action category predictions in the anchor-free branch further reduced the performance of the mixed methods. Our BDRC-Net uses a more elegant merging strategy to address the dependency on handcrafted anchors in existing mixed methods while improving detection performance. At the same time, BDRC-Net further enhances the accuracy of action predictions by predicting reliable action categories.

III. METHOD

This section elaborates on the proposed framework. As shown in Fig. 3, given an untrimmed video, we extract snippet features through the feature encoder. Moreover, a multi-scale backbone is used to obtain multi-scale features. Next, in the detection head, BDM and the classification module predict each snippet’s action boundaries and categories based on multi-scale features. In contrast, RCM directly predicts the action categories contained in the entire video based on the snippet features. Finally, the detection results are obtained by post-processing the results of RCM and the detection head.

A. Problem Definition

Given an untrimmed video V , we segment the video sequence into T non-overlapping snippets to reduce computational complexity. Specifically, each snippet consists of a small number of consecutive frames. For the t -th snippet, we obtain a D -dimensional spatio-temporal feature representation $\mathbf{F}_v(t)$ through a pre-trained 3D convolutional network. Collecting the

features of all snippets together, we denote it as $\mathbf{F}_v \in \mathbb{R}^{T \times D}$. The annotations of all action instances in V are denoted as $\Psi^g = \{\psi_n^g \mid \psi_n^g = (y_{s,n}^g, y_{e,n}^g, y_{c,n}^g)\}_{n=1}^{N_g}$, where N_g is the number of action instances, and $y_{s,n}^g$, $y_{e,n}^g$, $y_{c,n}^g$ represent the start time, end time, and action label of the n -th action instance, respectively. The goal of TAD is to use \mathbf{F}_v to locate starting and ending times of action instances in the untrimmed video and predict their action categories.

B. Multi-Scale Backbone (MSB)

In this subsection, we briefly describe the method for obtaining and representing multi-scale features in a general multi-scale backbone (MSB). An MSB usually consists of multiple base blocks, wherein the first layer of each base block, the video features are downsampled by a factor of 2 in the temporal dimension. Then some convolutional layers or transformer layers are used to model the spatio-temporal context. The modeled features are used to input the detection head and the next layer of the base block. Therefore, for an L -layer MSB, we obtain a set of features: $\{\mathbf{F}_l \mid \mathbf{F}_l \in \mathbb{R}^{T_l \times D_l}\}_{l=1}^L$, where \mathbf{F}_l denotes the video features output from the l -th layer, and T_l , D_l represent the temporal length and dimension of the features at that layer. Specifically, each base block in MSB downsamples the feature's length but keeps the feature's dimension unchanged, so all feature dimensions are the same in MSB. Since the detection head shares weights on the features of each layer in MSB, we use $\mathbf{F}_{ms} \in \mathbb{R}^{T_{ms} \times D_{ms}}$ to represent multi-scale features for clarity in the following parts. Here, \mathbf{F}_{ms} is the concatenation of $\{\mathbf{F}_l\}_{l=1}^L$ along the temporal dimension, $T_{ms} = \sum_{l=1}^L T_l$, and $D_{ms} = D_l$. Our proposed methods, BDM and RCM, are suitable for any MSB, and we verify their robustness on different MSB in the experimental section.

C. Boundary Discretization Module (BDM)

As described in Sec. I, although mixed methods can utilize the advantages of anchor-based and anchor-free methods, they still suffer from the issues of brute-force merging, handcrafted anchors design, and excessive false positives in action category predictions. To address the issues of brute-force merging and handcrafted anchors design, we propose BDM, which merges anchor-based and anchor-free methods more elegantly. In BDM, we predict action boundaries as a Coarse-Classification Sub-Module (CCSM) and a Refinement Regression Sub-Module (RRSM). CCSM discretizes the distance of action boundaries into multiple bins and predicts which bin the action boundaries belong to. Since each bin represents a small continuous time period, we use the center position of the bin as the predicted coarse boundary. Although this method enhances the stability of boundary predictions, it sacrifices some flexibility. Therefore, we subsequently propose that RRSM refine the coarse boundaries by regressing the distance between the predicted coarse and actual action boundaries.

CCSM. The purpose of CCSM is to predict the coarse action boundaries. As shown in Fig. 4, CCSM lays out W bins in both starting and ending directions for the t -th snippet and predicts which bin the action boundaries belongs to. Given

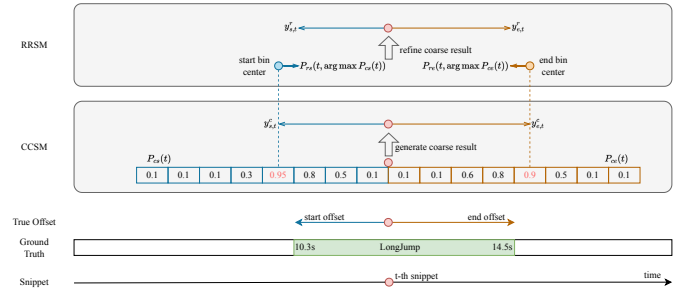


Fig. 4. BDM. For the t -th snippet, CCSM selects the center position of the bin with the highest predicted probability as a coarse prediction of the action boundary. Subsequently, RRSM regresses the distance between the coarse prediction and the actual boundary to obtain refined boundary prediction.

\mathbf{F}_{ms} , mathematically, we have $(P_{cs}, P_{ce}) = \Phi_{ccsm}(\mathbf{F}_{ms})$, where Φ_{ccsm} represents the CCSM, and $P_{cs} \in \mathbb{R}^{T_{ms} \times W}$, $P_{ce} \in \mathbb{R}^{T_{ms} \times W}$ represents the predictions of starting and ending position, respectively. For the t -th snippet, the predicted starting and ending positions are denoted as $P_{cs}(t)$ and $P_{ce}(t)$. As shown in Fig. 4, we use the center position of the bin with the maximum probability in $P_{cs}(t)$ and $P_{ce}(t)$ as the coarse prediction. Denote the coverage length of each bin as b , we can obtain the coarse prediction $y_t^c = (y_{s,t}^c, y_{e,t}^c)$ at the t -th snippet with the following equations:

$$\begin{cases} y_{s,t}^c = (t - (\arg \max P_{cs}(t) \times b + b/2)) \times S(t) \\ y_{e,t}^c = (t + (\arg \max P_{es}(t) \times b + b/2)) \times S(t) \end{cases} \quad (1)$$

Where $S(t)$ is the scaling factor of t -th snippet, if the snippet belongs to the l -th level of the MSB, then $S(t) = 2^{l-1}$.

RRSM. CCSM representing the center position of each bin as the boundary results in too coarse predictions, making it difficult to locate action boundaries precisely. Therefore, to further refine the coarse boundaries, RRSM is used to regress the distance between the coarse and actual action boundaries. Given \mathbf{F}_{ms} , we have $(P_{rs}, P_{re}) = \Phi_{rrsm}(\mathbf{F}_{ms})$, where Φ_{rrsm} represents the RRSM, $P_{rs} \in \mathbb{R}^{T_{ms} \times W}$, $P_{re} \in \mathbb{R}^{T_{ms} \times W}$ represents the regression predictions of starting and ending distance, respectively. For the t -th snippet, the regression predictions for starting and ending distances corresponding to each bin are denoted as $P_{rs}(t)$ and $P_{re}(t)$, respectively. As shown in Fig. 4, after obtaining the coarse result through CCSM on the t -th snippet, the corresponding regression predictions on starting and ending bins are used to refine the coarse result. Finally, we obtain the refined result $y_t^r = (y_{s,t}^r, y_{e,t}^r)$ on the t -th snippet with the following equations:

$$\begin{cases} y_{s,t}^r = y_{s,t}^c - P_{rs}(t, \arg \max P_{cs}(t)) \\ y_{e,t}^r = y_{e,t}^c + P_{re}(t, \arg \max P_{es}(t)) \end{cases} \quad (2)$$

D. Reliable Classification Module (RCM)

The purpose of RCM is to predict the reliable action categories that occur throughout the entire video to filter out false positives caused by traditional snippet-level action classification. In this sub-section, we first introduce the typical snippet-level action classification and then provide a detailed description of the workflow of RCM.

Snippet-level action classification. Existing one-stage anchor-free methods use snippet-level action classification to predict the action categories to which each input snippet belongs. Let the number of action categories be K , mathematically we have: $P_{sc} = \Phi_{sc}(\mathbf{F}_{ms})$. Here, Φ_{sc} is the snippet-level classification network, and $P_{sc} \in \mathbb{R}^{T_{ms} \times K}$ is the action classification probabilities. Furthermore, we denote t -th snippet's corresponding prediction probabilities as $P_{sc}(t)$. If the prediction probability $P_{sc}(t, k)$ of the k -th action category on the t -th snippet is greater than λ_{cls} , this indicates that k -th action occurs on that snippet. It should be noted that there may be multiple action categories with prediction probabilities greater than λ_{cls} on the given snippet, resulting in multiple predicted action categories for that snippet where λ_{cls} is a hyper-parameter of predict action categories. While improving the recall rate of action instances, this method also increases the false positives in the predicted results.

RCM. To reduce false positives caused by snippet-level action classification, RCM is proposed. RCM predicts reliable video-level action categories by aggregating the prediction results of discriminative snippets. Unlike BDM and snippet-level classification, RCM directly uses snippet features \mathbf{F}_v as input instead of using multi-scale features \mathbf{F}_{ms} . In snippet-level classification, \mathbf{F}_{ms} is used to classify each snippet's actions. However, the snippet-level classification results on non-discriminative segments, as shown in Fig. 2, are untrustworthy. Even if these results can help us find the location of action instances with high activation values, the predicted action categories may be wrong. In contrast, the video-level action predictions of RCM do not need to consider the location of action instances. It only needs to aggregate the predictions of some highly discriminative snippets to obtain reliable action categories for the entire video. Therefore, using \mathbf{F}_v in RCM can avoid the mutual disturbance caused by inconsistencies with the snippet-level classification target when using \mathbf{F}_{ms} .

Given the snippet feature \mathbf{F}_v , RCM first predicts the action categories for each snippet. Mathematically, we have: $P_{rc} = \Phi_{rcm}(\mathbf{F}_v)$. Here, Φ_{rcm} is the RCM network, and $P_{rc} \in \mathbb{R}^{T \times K}$ is the predicted action probabilities for each snippet. Specifically, to obtain reliable video-level categories, RCM selects the top- N_v snippets with the highest confidence score as highly discriminative snippets. Moreover, we use P_{rc} as the confidence score. In contrast, the remaining snippets are denoted as non-discriminative snippets. In RCM, only the highly discriminative snippets are used to predict the probabilities $P_{vl} \in \mathbb{R}^K$ of video-level categories. Especially, $P_{vl}(k)$ is the probability of the k -th action occurring in the video, which is calculated by the following equation:

$$P_{vl}(k) = \max_{\substack{\mathbf{M} \subset P_{rc}(:,k) \\ |\mathbf{M}|=N_v}} \frac{1}{N_v} \sum_{r=1}^{N_v} \mathbf{M}(r) \quad (3)$$

Where, $\mathbf{M} \in \mathbb{R}^{N_v}$ is the set of probability values for the top- N_v snippets with the highest predicted probabilities for the k -th action category. Finally, we obtain a reliable set of action categories $y^{vid} = \{k \mid P_{vl}(k) > \lambda_{vid}\}$, where λ_{vid} is a hyper-parameter used to obtain action categories based on prediction probabilities.

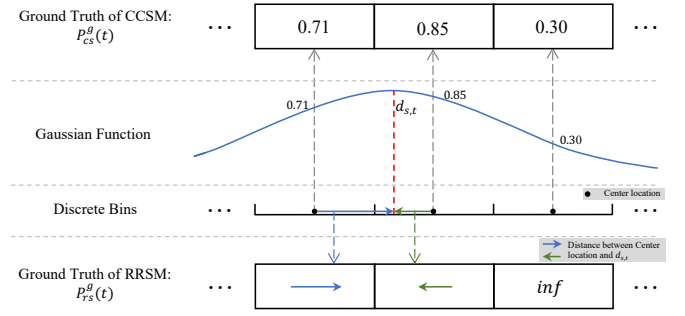


Fig. 5. Label assignment in BDM. For the starting bin on the t -th snippet, firstly, the distance $d_{s,t}$ between snippet t and the starting boundary is computed. Then, a Gaussian function with mean and variance as $d_{s,t}$ and σ is used to assign labels in CCSM. Specifically, the label for each bin in CCSM is the value of its central position on the Gaussian function. We further assign labels for RRSM, where the label for each bin on RRSM is the distance between $d_{s,t}$ and its center position.

IV. TRAINING AND INFERENCE

In this section, we provide detailed explanations of the training and inference processes for the proposed method.

A. Training

In the training section, we first introduce label assignment and then compute the loss function based on the results of label assignment and the model prediction in Sec. III.

Label Assignment. Given the annotation set $\Psi^g = \{\psi_n^g \mid \psi_n^g = (y_{s,n}^g, y_{e,n}^g, y_{c,n}^g)\}_{n=1}^{N_g}$ for video V , we generate corresponding ground truths for CCSM, RRSM, snippet-level classification and RCM. The ground truth of the starting and ending bins in CCSM is denoted as $P_{cs}^g \in \mathbb{R}^{T_{ms} \times W}$ and $P_{ce}^g \in \mathbb{R}^{T_{ms} \times W}$, while the ground truth of the starting and ending bins in RRSM is denoted as $P_{rs}^g \in \mathbb{R}^{T_{ms} \times W}$ and $P_{re}^g \in \mathbb{R}^{T_{ms} \times W}$. For snippet-level classification and RCM, the ground truth is denoted as $P_{sc}^g \in \mathbb{R}^{T_{ms} \times K}$ and $P_{vl}^g \in \mathbb{R}^K$, respectively. In particular, the initial values of P_{cs}^g , P_{ce}^g , P_{sc}^g , and P_{vl}^g are set to 0, while the initial values of P_{rs}^g and P_{re}^g are set to inf.

As shown in Fig. 5, if the t -th snippet belongs to the annotation of the n -th action instance, i.e., $y_{s,n}^g \leq t \leq y_{e,n}^g$, then the ground truth for snippet-level classification corresponding to this snippet is $P_{sc}^g(t, y_{c,n}^g) = 1$. Furthermore, the distance between this snippet and the starting position of the n -th annotation is denoted as $d_{s,t}$, where $d_{s,t} = t - y_{s,n}^g / S(t)$. We assign ground truth to each starting bin $P_{cs}^g(t, :)$ of CCSM on the t -th snippet by convolving a Dirac delta function centered at $d_{s,t}$ with a Gaussian of fixed variance σ . Specifically, the ground truth of the w -th bin in $P_{cs}^g(t)$ denote as $P_{cs}^g(t, w)$, mathematically, we have:

$$P_{cs}^g(t, w) = \frac{1}{\sigma\sqrt{2\pi}} e^{-\frac{1}{2}(\frac{x_w - d_{s,t}}{\sigma})^2} \quad (4)$$

Where x_w is the center position of the w -th starting bin on the t -th snippet, which is $x_w = w \times b + b/2$. We further assign ground truth to each starting bin $P_{rs}^g(t, :)$ of RRSM on the t -th snippet. Specifically, for the w -th starting bin on this snippet, if $P_{cs}^g(t, w) > \lambda_{rs}$, then its ground truth $P_{rs}^g(t, w)$ is the

distance between its center position and the starting boundary of the n -th annotation: $P_{rs}^g(t, w) = (d_{s,t} - x_w) \times S(t)$. Similarly, we assign the corresponding ground truths $P_{ce}^g(t)$ and $P_{re}^g(t)$ of CCSM and RRSM to the ending bins of the t -th snippet.

After assigning ground truth to all snippets, we obtain P_{cs}^g , P_{ce}^g , P_{rs}^g , P_{re}^g , and P_{sc}^g . RCM is used to predict the action categories that occur in the video; the ground truth P_{vl}^g can be obtained by aggregating P_{sc}^g . Specifically, $P_{vl}^g(k) = \mathbb{I}[\sum_{t=1}^{T_{ms}} P_{sc}^g(t, k) > 0]$, where $\mathbb{I}[\cdot]$ is the indicator function, and $P_{vl}^g(k)$ is the label of k -th action in P_{vl}^g .

Loss Function. Given the predictions P_{cs} and P_{ce} of CCSM and their corresponding ground truths P_{cs}^g and P_{ce}^g , the loss function \mathcal{L}_{ccsm} of CCSM is calculated by the following equation:

$$\mathcal{L}_{ccsm} = \frac{1}{\lambda_{norm}} \left(\sum_{t=1}^{T_{ms}} \sum_{w=1}^W (\mathcal{L}_{focal}(P_{cs}(t, w), P_{cs}^g(t, w)) + \mathcal{L}_{focal}(P_{ce}(t, w), P_{ce}^g(t, w))) \right) \quad (5)$$

Where \mathcal{L}_{focal} represents the focal loss [29], and λ_{norm} is the coefficient used to balance the loss.

For RRSM, we calculate the smooth L_1 loss \mathcal{L}_{sl} on all positive bins whose ground truths is non-inf, resulting in \mathcal{L}_{rrsm} :

$$\begin{aligned} \mathcal{L}_{rrsm} = \frac{1}{\lambda_{norm}} & \left(\sum_{t=1}^{T_{ms}} \sum_{w=1}^W (\mathbb{I}[P_{rs}^g(t, w) \neq \text{inf}] \right. \\ & \times \mathcal{L}_{sl}(P_{rs}(t, w), P_{rs}^g(t, w)) \\ & + \mathbb{I}[P_{re}^g(t, w) \neq \text{inf}] \\ & \times \mathcal{L}_{sl}(P_{re}(t, w), P_{re}^g(t, w))) \end{aligned} \quad (6)$$

Where $\mathbb{I}[\cdot]$ is the indicator function.

The cross-entropy loss \mathcal{L}_{ce} is used to calculate the snippet-level action classification loss \mathcal{L}_{cls} and the video-level classification loss \mathcal{L}_{rcm} of RCM:

$$\begin{aligned} \mathcal{L}_{cls} &= \frac{1}{\lambda_{norm}} \sum_{t=1}^{T_{ms}} \sum_{k=1}^K \mathcal{L}_{ce}(P_{sc}(t, k), P_{sc}^g(t, k)) \\ \mathcal{L}_{rcm} &= \frac{1}{\lambda_{norm}} \sum_{k=1}^K \mathcal{L}_{ce}(P_{vl}(k), P_{vl}^g(k)) \end{aligned} \quad (7)$$

Finally, we calculate the sum of \mathcal{L}_{ccsm} , \mathcal{L}_{rrsm} , \mathcal{L}_{cls} , and \mathcal{L}_{rcm} to obtain the overall loss \mathcal{L} of our model:

$$\mathcal{L} = \mathcal{L}_{ccsm} + \mathcal{L}_{rrsm} + \mathcal{L}_{cls} + \mathcal{L}_{rcm} \quad (8)$$

B. Inference

Given an untrimmed video, we obtain the video-level action category results in y^{vid} using RCM as described in Sec. III-D. Firstly, we collect a set of all possible locations that may contain actions:

$$\Psi^{lo} = \{(t_i, k_i) \mid P_{sc}(t_i, k_i) > \lambda_{cls} \wedge k_i \in y^{vid}\}_{i=1}^{N_p} \quad (9)$$

Where t_i and k_i respectively represent the snippet index and action category index corresponding to the i -th predicted

location, and N_p is the total number of predicted locations. For location (t_i, k_i) in Ψ^{lo} , we take the boundary prediction $y_{t_i}^r = (y_{s,t_i}^r, y_{e,t_i}^r)$ of the corresponding snippet in Sec. III-C as the starting and ending boundary. Secondly, we calculate the confidence score for each location, where for the i -th prediction, the confidence score c_i is defined as:

$$c_i = P_{sc}(t_i, k_i) \times \sqrt{\max P_{cs}(t_i) \times \max P_{ce}(t_i)} \quad (10)$$

Finally, we obtain a set of predicted action instances: $\Psi = \{\psi_i \mid \psi_i = (y_{s,t_i}^r, y_{e,t_i}^r, k_i, c_i)\}_{i=1}^{N_p}$, where y_{s,t_i}^r , y_{e,t_i}^r , k_i , and c_i respectively represent the starting boundary, ending boundary, action category, and confidence score predicted for the i -th action instance. Specially, we use non-maximum suppression (NMS) [28] to suppress redundant action instances with high overlap.

V. EXPERIMENTS

We conducted extensive experiments on the THUMOS'14 [30], and ActivityNet-1.3 [31] benchmarks and compared our experimental results with previous works. Additionally, we performed extensive ablation experiments to validate our contributions.

A. Datasets

THUMOS'14 consists of 200 validation videos and 213 test videos with boundary annotations for 20 action categories. Following the standard setting [9], [12], [14], [17], [32], we train our model on the validation videos and evaluate its performance on the test videos.

ActivityNet-1.3 consists of 19,994 videos with action category annotations for 200 classes. It is split into train, validation, and test sets in a 2 : 1 : 1 ratio. We train our model on the train set and evaluate its performance on the validation set.

B. Evaluation Metric

Mean average precision (mAP) is a commonly used metric for evaluating the performance of TAD models and is measured using various temporal intersection over union (tIoU) thresholds. tIoU is calculated as the intersection over the union between two temporal boundaries. To evaluate the model's performance, mAP computes the mean of average precision scores across all action categories using a given tIoU threshold.

C. Implementation Details

For the feature encoder, we divide every 16 frames into one snippet and use a pre-trained two-stream I3D [33] network on Kinetics [33] to extract snippet features. Our method is suitable for any existing multi-scale backbone (MSB). Specifically, we conduct experiments on MSB implemented in ActionFormer [14], which has achieved excellent performance, and the MSB of A2Net [17], a state-of-the-art mixed method. Our CCSM, RRSM, and snippet-level classification are built using three temporal convolution layers with consistent parameter settings, including kernel size, stride, padding, and dimension, which

TABLE II

TEMPORAL ACTION DETECTION RESULTS ON THUMOS'14, MEASURED BY MAP AT DIFFERENT TIOU THRESHOLDS. THE BEST RESULT IN EACH COLUMN IS MARKED IN **RED**. COMMONLY USED FEATURE ENCODERS INCLUDE: C3D [34], P3D [35], I3D [33], R(2+1)D [36], TSN [37], SF [38], AND VGG [39]. AVG 0.3: AVERAGE MAP UNDER TIOU THRESHOLDS [0.3 : 0.1 : 0.7]. AVG 0.5: AVERAGE MAP UNDER TIOU THRESHOLDS [0.5 : 0.1 : 0.9].

Type	Model	Feature	Venue	0.3	0.4	0.5	0.6	0.7	0.8	0.9	avg 0.3	avg 0.5
Anchor-Based	R-C3D [6]	C3D	ICCV 2017	44.8	35.6	28.9	-	-	-	-	-	-
	GTAN [40]	P3D	CVPR 2019	57.8	47.2	38.8	-	-	-	-	-	-
	PBR-Net [7]	I3D	AAAI 2020	58.5	54.6	51.3	41.8	29.5	-	-	47.1	-
	Gemini [41]	Gemini	TMM 2020	56.7	50.6	42.6	32.5	21.4	-	-	40.8	-
	STAN [42]	TSN+VGG	TMM 2021	67.5	61.0	51.7	-	-	-	-	-	-
	MUSES [43]	I3D	CVPR 2021	68.9	64.0	56.9	46.3	31.0	-	-	53.4	-
	TBOS [8]	I3D	CVPR 2021	63.2	58.5	54.8	44.3	32.4	-	-	50.6	-
	VSGN [44]	I3D	ICCV 2021	66.7	60.4	52.4	41.0	30.4	-	-	50.1	-
	RCL [45]	I3D	CVPR 2022	70.1	62.3	52.9	42.7	30.7	-	-	51.7	-
	SAC [46]	I3D	TIP 2022	69.3	64.8	57.6	47.0	31.5	-	-	54.0	-
Anchor-Free	DBG [47]	TSN	AAAI 2020	57.8	49.4	42.8	33.8	21.7	-	-	41.1	-
	G-TAD [23]	TSN	CVPR 2020	54.5	47.6	40.2	30.8	23.4	-	-	39.3	-
	AFSD [12]	I3D	CVPR 2021	67.3	62.4	55.5	43.7	31.1	-	-	52.0	-
	RTD-Net [48]	I3D	ICCV 2021	68.3	62.3	51.9	38.8	23.7	-	-	49.0	-
	E2E-TAD [49]	SF R50	CVPR 2022	69.4	64.3	56.0	46.4	34.9	-	-	54.2	-
	TAGS [32]	I3D	ECCV 2022	68.6	63.8	57.0	46.3	31.8	-	-	52.8	-
	STPT [50]	STPT	ECCV 2022	70.6	65.7	56.4	44.6	30.5	-	-	53.6	-
	ReAct [27]	TSN	ECCV 2022	69.2	65.0	57.1	47.8	35.6	-	-	55.0	-
	TadTR [51]	I3D	TIP 2022	74.8	69.1	60.1	46.6	32.8	-	-	56.7	-
	TAPP [52]	I3D	TMM 2022	76.1	72.0	64.2	-	-	-	-	-	-
	TAGS+GAP [53]	I3D	CVPR 2023	69.1	-	57.4	-	32.0	-	-	53.0	-
	ActionFormer [14]	I3D	ECCV 2022	82.1	77.8	71.0	59.4	43.9	23.4	4.1	66.8	40.4
	ActionFormer+GAP [53]	I3D	CVPR 2023	82.3	-	71.4	-	44.2	-	-	66.9	-
	AMNet [54]	I3D	WACV 2023	76.7	73.1	66.8	57.2	42.7	-	-	63.3	-
	Self-DETR [55]	I3D	ICCV 2023	74.6	69.5	60.0	47.6	31.8	-	-	56.7	-
	MENet [56]	R(2+1)D	ICCV 2023	70.7	65.3	58.8	49.1	34.0	-	-	55.6	-
	EAC [57]	I3D	TMM 2023	81.6	78.4	72.2	59.0	44.5	-	-	67.1	-
	ASL [58]	I3D	ICCV 2023	83.1	79.0	71.7	59.7	45.8	-	-	67.9	-
	TriDet [59]	I3D	CVPR 2023	83.6	80.1	72.9	62.4	47.4	26.1	5.7	69.3	42.9
Mixed	PCAD [15]	C3D	TOMM 2020	52.8	47.1	39.2	-	-	-	-	-	-
	MGG [16]	TSN	CVPR 2019	53.9	46.8	37.4	29.5	21.3	-	-	37.8	-
	A2Net [17]	I3D	TIP 2020	58.6	54.1	45.5	32.5	17.2	-	-	41.6	-
Mixed	A2Net+BDRC-Net	I3D	-	65.9	60.0	50.6	38.6	25.2	12.2	2.0	48.1	25.7
	ActionFormer+BDRC-Net	I3D	-	82.7	79.0	71.4	61.2	48.6	27.7	6.9	68.6	43.2
	TriDet+BDRC-Net	I3D	-	84.0	80.4	72.7	62.4	48.6	28.5	7.4	69.6	43.9

are set to 3, 1, 1, and 512, respectively. Expressly, for the prediction layer, the dimensions of CCSM, RRSN, and snippet-level classification are set to $2 \times W$, $2 \times W$, and K , respectively. For RCM, we use two temporal convolution layers with identical parameters for kernel size, stride, and padding, which are set to 3, 1, and 1, respectively. The dimension of the first and second layers are set to 512 and K , respectively. Furthermore, N_v is set as $T_{ms}/8$ to aggregate highly discriminative snippets. All hyper-parameters are determined by empirical grid search. For the bin, we set W and b to 8 and 0.25, respectively, and the σ used for label assignment of CCSM is set to $\sqrt{0.2}$. For the hyper-parameters λ_{vid} , λ_{rs} , and λ_{norm} , we set them to 0.1, 0.5, and 90, respectively. The hyper-parameter λ_{cls} follows the setting used in MSB, and we do not make any specific adjustments. During training, we train for 34 epochs on the THUMOS'14 dataset with a learning rate of $1e-4$ and batch size of 24 and decay the learning rate to $1e-5$ at the 30-th epoch. For the ActivityNet-1.3 dataset, we train for 15 epochs with a learning rate of $5e-4$ and batch size of 16. During inference, the NMS threshold is set to 0.2, and following the standard setting [14], [17], we keep up to 200 predict results per video based on the confidence score.

D. Main Results

THUMOS'14. On the THUMOS'14 dataset, we report the performance of our method and compare the results with previous works in Table II. It can be observed that our approach with TriDet backbone achieves an average mAP of 69.6%, surpassing the previous state-of-the-art method. When employing the A2Net backbone and the ActionFormer backbone, our approach similarly exhibits performance improvements compared to their counterparts. Notably, our method shows outstanding performance at high tIoU thresholds. Compared with state-of-the-art, our approach with TriDet backbone obtains performance gains of 1.2%, 2.4%, and 1.7% in $mAP@tIoU = 0.7$, $mAP@tIoU = 0.8$, and $mAP@tIoU = 0.9$, respectively. This phenomenon indicates that our method achieves more precise action boundaries.

ActivityNet-1.3. As shown in Table III, BDRC-Net exhibits similar characteristics on ActivityNet-1.3 as on THUMOS'14. Following previous methods [14], [23], [60], we use TSP [61] feature and multiply the extra action scores from UntrimmedNet [18] with the final confidence scores, referred to as BDRC-Net_post. Under this setting, BDRC-Net_post achieves the best result, outperforming ActionFormer by 1.2% in $mAP@tIoU = 0.9$. We also evaluate the performance

TABLE III

TEMPORAL ACTION DETECTION RESULTS ON ACTIVITYNET-1.3, MEASURED BY mAP AT DIFFERENT tIoU THRESHOLDS. THE BEST RESULT IN EACH COLUMN IS MARKED IN **RED**. AVG: AVERAGE mAP UNDER tIoU THRESHOLDS [0.5 : 0.05 : 0.95].

Type	Model	Feature	0.5	0.75	0.9	avg(%)
Anchor-Based	GTAN [40]	P3D	52.6	34.1	-	34.3
	PBR-Net [7]	I3D	53.9	34.9	-	35.0
	STAN [42]	TSN+VGG	35.9	21.3	-	19.8
	MUSES [43]	I3D	50.0	34.9	-	34.0
	TBOS [8]	I3D	57.8	37.6	-	35.0
	VSGN [44]	I3D	52.4	36.0	-	35.1
	RCL [45]	I3D	51.7	35.3	-	34.4
	SAC [46]	I3D	50.7	35.4	-	34.4
Anchor-Free	G-TAD [23]	TS	50.4	34.6	-	34.1
	AFSD [12]	I3D	52.4	34.3	-	34.4
	RTD-Net [48]	I3D	47.2	30.7	-	30.8
	E2E-TAD [49]	SlowFast	50.5	36.0	-	35.1
	TAGS [32]	I3D	56.3	36.8	-	36.5
	STPT [50]	STPT	51.4	33.7	-	33.4
	ReAct [27]	TSN	49.6	33.0	-	32.6
	TadTR [51]	I3D	52.8	37.1	-	36.1
	TAPP [52]	I3D	53.1	34.3	-	34.4
	TAGS+GAP [53]	I3D	56.7	37.2	-	36.7
	AMNet [54]	I3D	54.3	37.7	-	36.4
	EAC [57]	I3D	54.2	35.1	-	34.2
	ASL [58]	I3D	54.1	37.4	-	36.2
	Self-DETR [55]	I3D	52.3	33.7	-	33.8
	ActionFormer_multi [†] [14]	I3D	46.4	31.3	15.3	30.6
	ActionFormer_multi [†] [14]	TSP	52.1	34.9	16.9	34.2
	ActionFormer_post [14]	I3D	54.3	36.7	18.5	36.0
	ActionFormer_post [14]	TSP	54.7	37.8	18.6	36.6
Mixed	A2Net [17]	I3D	43.6	28.7	-	27.8
Mixed	BDRC-Net_multi	I3D	50.5	34.6	18.0	33.7
	BDRC-Net_multi	TSP	53.0	36.4	18.5	35.4
	BDRC-Net_post	I3D	54.5	37.9	20.0	36.8
	BDRC-Net_post	TSP	54.5	38.2	19.8	36.9

of BDRC-Net_post using the I3D feature, and our method again achieves the best result compared to other methods, improving upon the ActionFormer counterpart by 1.4% in $mAP@tIoU = 0.9$. Notably, when removing the extra action scores, referred to as BDRC-Net_multi, our method outperforms the ActionFormer counterpart by 1.6% and 2.7% in $mAP@tIoU = 0.9$ under TSP and I3D features, respectively. These comprehensive experiments demonstrate the outstanding performance of our method on the ActivityNet-1.3 dataset, confirming the excellent robustness ability of BDRC-Net.

E. Ablation Studies

In this section, we conduct multiple ablation studies on the THUMOS'14 dataset. These studies include comparisons with other mixed methods, an analysis of the effectiveness of each module in BDRC-Net, and an investigation of the impact of various hyper-parameters. Notably, we first implement a BDRC-Net baseline based on A2Net's MSB, the state-of-the-art mixed method. We then compare the performance of BDRC-Net with A2Net to verify the advantage of BDRC-Net over other mixed methods. Subsequently, we conduct further ablation studies based on this baseline.

Comparison with other mixed methods. To fairly validate the effectiveness of our method, we implement a BDRC-Net baseline based on A2Net's MSB. Moreover, we compare its performance with that of A2Net, which is currently the best-performing mixed method. As shown in Table IV, our reproduce A2Net exhibited better performance than the official implementation (*Row 1 vs. Row 2*). Moreover, our method significantly outperforms A2Net when only using BDM in BDRC-Net, with an improvement of 3.2% in average mAP

TABLE IV

ABLATION STUDIES ON THE EFFECTIVENESS OF EACH PART OF OUR FRAMEWORK ON THUMOS'14, INCLUDING CCSM, RRSN, AND RCM. A2Net[†]: OUR REPRODUCE.

Method	CCSM	RRSM	RCM	mAP@tIoU(%)			average mAP(%) [0.5 : 0.1 : 0.9]
				0.5	0.7	0.9	
A2Net				45.5	17.2	-	-
A2Net [†]				45.2	19.1	0.9	20.9
BDRC-Net			✓	46.4	19.4	0.9	21.4
	✓		✓	46.7	22.1	1.2	23.0
	✓	✓	✓	50.0	23.4	1.3	24.4
	✓	✓		47.2	23.8	1.9	24.1
	✓	✓	✓	50.6	25.2	2.0	25.7

(*Row 2 vs. Row 6*). When using both BDM and RCM, the performance improves due to the reliable classification predictions provided by RCM, which can reduce false positives in action category predictions. The average mAP improve by 4.2% compared to A2Net (*Row 2 vs. Row 7*).

Main components analysis. We demonstrate the effectiveness of our proposed components in BDRC-Net: BDM and RCM. Moreover, our experiments are based on A2Net's MSB. Specifically, BDM consists of CCSM and RRSN, and we have individually validated the efficacy of these two sub-modules. As described in Table IV, CCSM yields a 1.1% absolute improvement in average mAP (*Row 4*). This improvement primarily stems from CCSM's ability to locate coarse boundaries of actions through boundary discretization stably. Consequently, CCSM exhibits minimal performance gain at higher tIoU thresholds. To refine the coarse results obtained by CCSM, RRSN is introduced. RRSN offers a 1.1% absolute improvement in average mAP compared to CCSM (*Row 4 vs. Row 6*). Especially, RRSN significantly enhances at higher tIoU thresholds, such as a 1.7% and 0.7% improvement in $mAP@tIoU = 0.7$ and $mAP@tIoU = 0.9$, respectively. This demonstrates RRSN's capability to predict more precise action boundaries. Additionally, our RCM is employed to predict reliable video-level action categories for filtering false positives in snippet-level action predictions. Therefore, RCM can easily integrate into other action detectors. When integrated into A2Net, RCM contributes a 0.5% absolute improvement in average mAP (*Row 2 vs. Row 3*). Additionally, RCM yields average mAP improvements of 1.4% for CCSM and 1.6% for BDM, respectively (*Row 5 and Row 7*). The consistent and stable enhancements across different models robustly attest to the effectiveness of RCM.

Hyper-parameters. As mentioned in Sec. V-C, all the hyper-parameters in BDRC-Net are set through empirical search. In this section, we delve into the discussion on determining these hyper-parameters and their respective impact. All experiments are conducted on the THUMOS '14 dataset using A2Net's MSB.

As mentioned in Sec. IV-A, the parameter λ_{rs} is used to assign labels for RRSN. As the experimental results presented in Table V indicates, the best detection performance is achieved when taking an intermediate value for λ_{rs} . When λ_{rs} is decreased, it introduces many hard examples during RRSN loss computation, increasing the learning difficulty and declining performance. On the other hand, increasing λ_{rs} reduces the number of positive examples in RRSN, also

TABLE V

ABLATION STUDIES OF THE HYPER-PARAMETERS ON THUMOS'14 INCLUDE λ_{rs} , λ_{norm} , AND σ , WHICH ARE USED FOR LABEL ASSIGNMENT IN RRSN, SCALING LOSS, AND LABEL ASSIGNMENT IN CCSM, RESPECTIVELY.

Parameter	Value	mAP@tIoU(%)			average mAP(%) [0.5 : 0.1 : 0.9]
		0.5	0.7	0.9	
λ_{rs}	0.4	49.6	25.3	1.9	25.4
	0.5	50.6	25.2	2.0	25.7
	0.6	48.0	25.0	2.0	24.9
	0.7	46.1	21.8	1.3	22.9
λ_{norm}	80	47.7	24.8	1.8	24.4
	90	50.6	25.2	2.0	25.7
	100	50.4	24.9	1.8	25.5
σ	$\sqrt{0.1}$	48.5	23.9	1.8	24.5
	$\sqrt{0.2}$	50.6	25.2	2.0	25.7
	$\sqrt{0.3}$	49.1	25.4	1.8	25.0

TABLE VI

ABLATION STUDIES OF THE NUMBER OF BINS AND BIN COVERAGE ON THUMOS'14.

W	b	mAP@tIoU(%)			average mAP(%) [0.5 : 0.1 : 0.9]
		0.5	0.7	0.9	
4	0.25	48.1	24.4	1.8	24.4
	0.5	49.9	25.0	1.8	25.5
8	0.25	50.6	25.2	2.0	25.7
	0.5	48.1	22.9	1.6	23.9

leading to decreased performance.

In BDRC-Net, σ is used to assign labels for CCSM. At the same time, when calculating the loss function, we scale the loss using loss normalization λ_{norm} followed by ActionFormer [14]. As shown in the experimental results in Table V, BDRC-Net achieves optimal performance when σ and λ_{norm} are set to $\sqrt{0.2}$ and 90, respectively.

Ablation on the number and coverage length of bins.

We present the ablation results of the number and coverage range of bins in BDM, conducted on the THUMOS'14 dataset using A2Net's MSB. Table VI shows that the best result is achieved with $W = 8$ and $b = 0.25$. We also find that when $W = 4$, a value of $b = 0.5$ yielded better performance than $b = 0.25$. This is because, in A2Net, the maximum length of the ground truth in the last MSB's layer is 2. When $W \times b$ equals this length, all bins can encompass all possible boundaries, improving performance. When $W \times b$ exceeds this length, although it still covers all possible boundaries, the increased coverage length per bin decreases the accuracy of CCSM boundary predictions. Similarly, when $W \times b$ is less than the maximum ground truth length, bins cannot cover all action boundaries. While reducing the coverage length per bin enhances the accuracy of predicting shorter ground truth boundaries, it leads to poorer boundary prediction performance when the ground truth length exceeds $W \times b$, resulting in a performance decrease.

Confidence score. In Table VII, we present the impact of different confidence score calculation methods on detection performance. Accurate confidence scoring leads to a more precise ranking of detection results and is beneficial for practical applications of action detection. We observe that

TABLE VII

ABLATION STUDIES OF CONFIDENCE SCORE ON THUMOS'14. *score 1*: $P_{sc}(t_i, k_i)$; *score 2*: $P_{sc}(t_i, k_i) \times \max P_{cs}(t_i)$; *score 3*: $P_{sc}(t_i, k_i) \times \max P_{ce}(t_i)$; *score 4*: $P_{sc}(t_i, k_i) \times \max P_{cs}(t_i) \times \max P_{ce}(t_i)$; *score 5*: $P_{sc}(t_i, k_i) \times \sqrt{\max P_{cs}(t_i) \times \max P_{ce}(t_i)}$.

Method	mAP@tIoU(%)			average mAP(%) [0.5 : 0.1 : 0.9]
	0.5	0.7	0.9	
<i>score 1</i>	50.2	24.4	1.9	25.2
<i>score 2</i>	50.2	24.4	2.0	25.4
<i>score 3</i>	50.5	24.7	1.9	25.5
<i>score 4</i>	50.5	24.9	2.0	25.6
<i>score 5</i>	50.6	25.2	2.0	25.7

TABLE VIII

COMPARISON OF MODEL EFFICIENCY, IN TERMS OF INFERENCE TIME AND FLOPS. WE REPORT THE AVERAGE MAP ON THUMOS'14 AT tIoU THRESHOLDS RANGING FROM 0.5 TO 0.9 WITH INTERVALS OF 0.1.

Method	A2Net	BDRC-Net w/o RCM	BDRC-Net
Infe. Time / ms	7.6	7.5	7.7
FLOPs / G	1.24	1.20	1.24
average mAP(%) [0.5 : 0.1 : 0.9]	20.9	24.1	25.7

considering both snippet-level classification scores and the predicted probabilities of bins in BDM leads to better confidence scores (*score 4* and *score 5*). Furthermore, achieving optimal performance involves reducing the weight of bin prediction probabilities in the confidence score calculation (*score 5*). In contrast, *score 1*, *score 2*, and *score 3* only consider partial prediction probabilities, which reduces the quality of confidence scores and decreases performance.

F. Analysis

In this section, we analyze the model efficiency of BDRC-Net, the classification performance of RCM, and finally, provide visible results to demonstrate the precision of boundary predictions for BDRC-Net.

Model Efficiency. Model efficiency is an essential factor in practical applications. We compare the efficiency of A2Net and our proposed method on a single RTX 3090 GPU. The experimental results are shown in Table VIII. Compared to A2Net, BDRC-Net without RCM exhibits lower inference time and FLOPs while significantly improving average mAP ($\uparrow 3.2\%$). When RCM is added, BDRC-Net experiences a slight increase in inference time but achieves further performance improvement (1.6% increase in average mAP compared to without RCM). In summary, our proposed BDRC-Net is suitable for considering both efficiency and effectiveness.

RCM analysis. To verify whether RCM produces reliable classification results, we compare the $F1$ scores of action classification among A2Net, A2Net[†], A2Net[†] with RCM, BDRC-Net without RCM, and BDRC-Net. The experimental results are shown in Table IX. It can be observed that when without RCM, both A2Net and BDRC-Net have lower $F1$ scores, demonstrating that the classification performance is poor without RCM. When RCM is added, it provides reliable

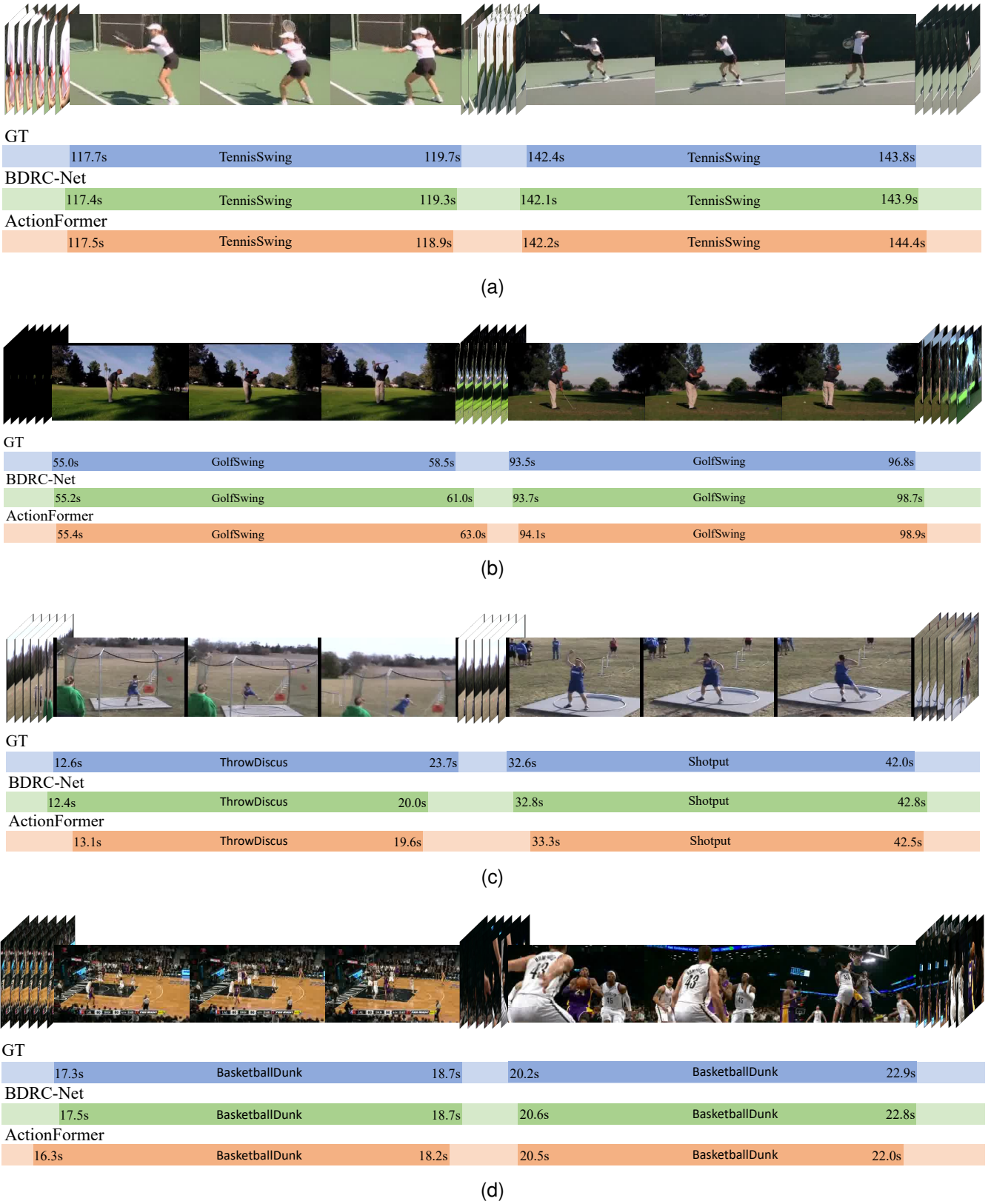


Fig. 6. Visualizations of the action detection results for ActionFormer and BDRC-Net on THUMOS'14 dataset. (a) TennisSwing. (b) GolfSwing. (c) ThrowDiscus and Shotput. (d) BasketballDunk.

video-level action predictions and filters out a large number of false positives in their prediction results. As a result, the $F1$ scores of both A2Net and BDRC-Net significantly increase.

Visualization results. To demonstrate the improvement of our framework, we present some examples in Fig. 6 that compare our method with ActionFormer, on the THUMOS'14

TABLE IX
COMPARE THE $F1$ SCORE OF ACTION CATEGORIES IN THE DETECTION
RESULTS OF DIFFERENT MODELS ON THE THUMOS'14 DATASET.
A2Net[†]: OUR REPRODUCE.

Method	A2Net	A2Net [†]	A2Net [†] w/ RCM	BDRC-Net w/o RCM	BDRC-Net
F1	0.18	0.17	0.71	0.25	0.79

dataset. It can be observed that our method can generate highly precise and reliable action boundaries, and the optimized temporal boundaries correspond better to actual action instances. Furthermore, our method performs well in detecting action instances within scenarios involving multiple action categories (Fig. 6c) and adapts effectively to various complex contexts (Fig. 6d).

VI. CONCLUSION

In this paper, we propose a novel method, BDRC-Net, for temporal action detection task. BDRC-Net consists of a boundary discretization module (BDM) and a reliable classification module (RCM). BDM elegantly integrates anchor-based and anchor-free approaches through boundary discretization, achieving a superior mixed method that mitigates brute-force merging and handcrafted anchors design in existing mixed methods. In detail, BDM first predicts stable but coarse action boundaries using a coarse classification sub-module (CCSM). Then, the refined regression sub-module (RRSM) is used to refine the coarse results obtained from CCSM, generating more precise action boundaries. Moreover, RCM filters false positives in snippet-level action category predictions by predicting reliable video-level action categories, thereby enhancing the accuracy of the detection results. Extensive experiments demonstrate that our method achieves state-of-the-art on THUMOS'14 and ActivityNet-1.3.

REFERENCES

- [1] Q. Li, J. Chen, Q. Xie, and X. Han, "Video summarization for event-centric videos," *Neural Networks*, 2023.
- [2] H. Zhang and C.-W. Ngo, "A fine granularity object-level representation for event detection and recounting," *IEEE Transactions on Multimedia*, vol. 21, no. 6, pp. 1450–1463, 2018.
- [3] K. Kumar and D. D. Shrimankar, "F-des: Fast and deep event summarization," *IEEE Transactions on Multimedia*, vol. 20, no. 2, pp. 323–334, 2017.
- [4] S. Ma, J. Zhang, S. Sclaroff, N. Ikizler-Cinbis, and L. Sigal, "Space-time tree ensemble for action recognition and localization," *International Journal of Computer Vision*, vol. 126, pp. 314–332, 2018.
- [5] T. Lin, X. Zhao, and Z. Shou, "Single shot temporal action detection," in *Proceedings of the 25th ACM international conference on Multimedia*, 2017, pp. 988–996.
- [6] H. Xu, A. Das, and K. Saenko, "R-c3d: Region convolutional 3d network for temporal activity detection," in *Proceedings of the IEEE international conference on computer vision*, 2017, pp. 5783–5792.
- [7] Q. Liu and Z. Wang, "Progressive boundary refinement network for temporal action detection," in *Proceedings of the AAAI conference on artificial intelligence*, vol. 34, no. 07, 2020, pp. 11 612–11 619.
- [8] Z. Li and L. Yao, "Three birds with one stone: Multi-task temporal action detection via recycling temporal annotations," in *Proceedings of the IEEE/CVF Conference on Computer Vision and Pattern Recognition*, 2021, pp. 4751–4760.
- [9] F. Cheng and G. Bertasius, "Tallformer: Temporal action localization with a long-memory transformer," in *Computer Vision—ECCV 2022: 17th European Conference, Tel Aviv, Israel, October 23–27, 2022, Proceedings, Part XXXIV*. Springer, 2022, pp. 503–521.
- [10] Y. Zhao, Y. Xiong, L. Wang, Z. Wu, X. Tang, and D. Lin, "Temporal action detection with structured segment networks," in *Proceedings of the IEEE international conference on computer vision*, 2017, pp. 2914–2923.
- [11] T. Lin, X. Zhao, H. Su, C. Wang, and M. Yang, "Bsn: Boundary sensitive network for temporal action proposal generation," in *Proceedings of the European conference on computer vision (ECCV)*, 2018, pp. 3–19.
- [12] C. Lin, C. Xu, D. Luo, Y. Wang, Y. Tai, C. Wang, J. Li, F. Huang, and Y. Fu, "Learning salient boundary feature for anchor-free temporal action localization," in *Proceedings of the IEEE/CVF Conference on Computer Vision and Pattern Recognition*, 2021, pp. 3320–3329.
- [13] J. Hu, L. Zhuang, B. Wang, T. Ge, Y. Jiang, H. Li *et al.*, "Estimation of reliable proposal quality for temporal action detection," *arXiv preprint arXiv:2204.11695*, 2022.
- [14] C.-L. Zhang, J. Wu, and Y. Li, "Actionformer: Localizing moments of actions with transformers," in *European Conference on Computer Vision*. Springer, 2022, pp. 492–510.
- [15] S. Zhu, X. Yang, J. Yu, Z. Fang, M. Wang, and Q. Huang, "Proposal complementary action detection," *ACM Transactions on Multimedia Computing, Communications, and Applications (TOMM)*, vol. 16, no. 2s, pp. 1–12, 2020.
- [16] Y. Liu, L. Ma, Y. Zhang, W. Liu, and S.-F. Chang, "Multi-granularity generator for temporal action proposal," in *Proceedings of the IEEE/CVF conference on computer vision and pattern recognition*, 2019, pp. 3604–3613.
- [17] L. Yang, H. Peng, D. Zhang, J. Fu, and J. Han, "Revisiting anchor mechanisms for temporal action localization," *IEEE Transactions on Image Processing*, vol. 29, pp. 8535–8548, 2020.
- [18] L. Wang, Y. Xiong, D. Lin, and L. Van Gool, "Untrimmednets for weakly supervised action recognition and detection," in *Proceedings of the IEEE conference on Computer Vision and Pattern Recognition*, 2017, pp. 4325–4334.
- [19] B. He, X. Yang, L. Kang, Z. Cheng, X. Zhou, and A. Shrivastava, "Asm-loc: Action-aware segment modeling for weakly-supervised temporal action localization," in *Proceedings of the IEEE/CVF conference on computer vision and pattern recognition*, 2022, pp. 13 925–13 935.
- [20] Y. Zhao, H. Zhang, Z. Gao, W. Gao, M. Wang, and S. Chen, "A novel action saliency and context-aware network for weakly-supervised temporal action localization," *IEEE Transactions on Multimedia*, 2023.
- [21] Y. Huang, Q. Dai, and Y. Lu, "Decoupling localization and classification in single shot temporal action detection," in *2019 IEEE International Conference on Multimedia and Expo (ICME)*. IEEE, 2019, pp. 1288–1293.
- [22] Y.-W. Chao, S. Vijayanarasimhan, B. Seybold, D. A. Ross, J. Deng, and R. Sukthankar, "Rethinking the faster r-cnn architecture for temporal action localization," in *proceedings of the IEEE conference on computer vision and pattern recognition*, 2018, pp. 1130–1139.
- [23] M. Xu, C. Zhao, D. S. Rojas, A. Thabet, and B. Ghanem, "G-tad: Sub-graph localization for temporal action detection," in *Proceedings of the IEEE/CVF Conference on Computer Vision and Pattern Recognition*, 2020, pp. 10 156–10 165.
- [24] S. Ren, K. He, R. Girshick, and J. Sun, "Faster r-cnn: Towards real-time object detection with region proposal networks," *Advances in neural information processing systems*, vol. 28, 2015.
- [25] T. Lin, X. Liu, X. Li, E. Ding, and S. Wen, "Bmn: Boundary-matching network for temporal action proposal generation," in *Proceedings of the IEEE/CVF international conference on computer vision*, 2019, pp. 3889–3898.
- [26] P. Chen, C. Gan, G. Shen, W. Huang, R. Zeng, and M. Tan, "Relation attention for temporal action localization," *IEEE Transactions on Multimedia*, vol. 22, no. 10, pp. 2723–2733, 2019.
- [27] D. Shi, Y. Zhong, Q. Cao, J. Zhang, L. Ma, J. Li, and D. Tao, "React: Temporal action detection with relational queries," in *European conference on computer vision*. Springer, 2022, pp. 105–121.
- [28] A. Rosenfeld and M. Thurston, "Edge and curve detection for visual scene analysis," *IEEE Transactions on computers*, vol. 100, no. 5, pp. 562–569, 1971.
- [29] T.-Y. Lin, P. Goyal, R. Girshick, K. He, and P. Dollár, "Focal loss for dense object detection," in *Proceedings of the IEEE international conference on computer vision*, 2017, pp. 2980–2988.
- [30] H. Idrees, A. R. Zamir, Y.-G. Jiang, A. Ghorban, I. Laptev, R. Sukthankar, and M. Shah, "The thumos challenge on action recognition for videos "in the wild"," *Computer Vision and Image Understanding*, vol. 155, pp. 1–23, 2017.
- [31] F. Caba Heilbron, V. Escorcia, B. Ghanem, and J. Carlos Niebles, "Activitynet: A large-scale video benchmark for human activity under-

- standing,” in *Proceedings of the IEEE Conference on Computer Vision and Pattern Recognition (CVPR)*, June 2015.
- [32] S. Nag, X. Zhu, Y.-Z. Song, and T. Xiang, “Proposal-free temporal action detection via global segmentation mask learning,” in *European Conference on Computer Vision*, 2022, pp. 645–662.
- [33] J. Carreira and A. Zisserman, “Quo vadis, action recognition? a new model and the kinetics dataset,” in *proceedings of the IEEE Conference on Computer Vision and Pattern Recognition*, 2017, pp. 6299–6308.
- [34] D. Tran, L. Bourdev, R. Fergus, L. Torresani, and M. Paluri, “Learning spatiotemporal features with 3d convolutional networks,” in *Proceedings of the IEEE international conference on computer vision*, 2015, pp. 4489–4497.
- [35] Z. Qiu, T. Yao, and T. Mei, “Learning spatio-temporal representation with pseudo-3d residual networks,” in *proceedings of the IEEE International Conference on Computer Vision*, 2017, pp. 5533–5541.
- [36] D. Tran, H. Wang, L. Torresani, J. Ray, Y. LeCun, and M. Paluri, “A closer look at spatiotemporal convolutions for action recognition,” in *Proceedings of the IEEE conference on Computer Vision and Pattern Recognition*, 2018, pp. 6450–6459.
- [37] L. Wang, Y. Xiong, Z. Wang, Y. Qiao, D. Lin, X. Tang, and L. Van Gool, “Temporal segment networks: Towards good practices for deep action recognition,” in *European conference on computer vision*. Springer, 2016, pp. 20–36.
- [38] C. Feichtenhofer, H. Fan, J. Malik, and K. He, “Slowfast networks for video recognition,” in *Proceedings of the IEEE/CVF international conference on computer vision*, 2019, pp. 6202–6211.
- [39] K. Simonyan and A. Zisserman, “Very deep convolutional networks for large-scale image recognition,” *arXiv preprint arXiv:1409.1556*, 2014.
- [40] F. Long, T. Yao, Z. Qiu, X. Tian, J. Luo, and T. Mei, “Gaussian temporal awareness networks for action localization,” in *Proceedings of the IEEE/CVF Conference on Computer Vision and Pattern Recognition*, 2019, pp. 344–353.
- [41] Y. Zhou, R. Wang, H. Li, and S.-Y. Kung, “Temporal action localization using long short-term dependency,” *IEEE Transactions on Multimedia*, vol. 23, pp. 4363–4375, 2020.
- [42] C. Sun, H. Song, X. Wu, Y. Jia, and J. Luo, “Exploiting informative video segments for temporal action localization,” *IEEE Transactions on Multimedia*, vol. 24, pp. 274–287, 2021.
- [43] X. Liu, Y. Hu, S. Bai, F. Ding, X. Bai, and P. H. Torr, “Multi-shot temporal event localization: a benchmark,” in *Proceedings of the IEEE/CVF Conference on Computer Vision and Pattern Recognition*, 2021, pp. 12 596–12 606.
- [44] C. Zhao, A. K. Thabet, and B. Ghanem, “Video self-stitching graph network for temporal action localization,” in *Proceedings of the IEEE/CVF International Conference on Computer Vision*, 2021, pp. 13 658–13 667.
- [45] Q. Wang, Y. Zhang, Y. Zheng, and P. Pan, “Rcl: Recurrent continuous localization for temporal action detection,” in *Proceedings of the IEEE/CVF Conference on Computer Vision and Pattern Recognition*, 2022, pp. 13 566–13 575.
- [46] L. Yang, J. Han, T. Zhao, N. Liu, and D. Zhang, “Structured attention composition for temporal action localization,” *IEEE Transactions on Image Processing*, 2022.
- [47] C. Lin, J. Li, Y. Wang, Y. Tai, D. Luo, Z. Cui, C. Wang, J. Li, F. Huang, and R. Ji, “Fast learning of temporal action proposal via dense boundary generator,” in *Proceedings of the AAAI conference on artificial intelligence*, vol. 34, no. 07, 2020, pp. 11 499–11 506.
- [48] J. Tan, J. Tang, L. Wang, and G. Wu, “Relaxed transformer decoders for direct action proposal generation,” in *Proceedings of the IEEE/CVF international conference on computer vision*, 2021, pp. 13 526–13 535.
- [49] X. Liu, S. Bai, and X. Bai, “An empirical study of end-to-end temporal action detection,” in *Proceedings of the IEEE/CVF Conference on Computer Vision and Pattern Recognition*, 2022, pp. 20 010–20 019.
- [50] Y. Weng, Z. Pan, M. Han, X. Chang, and B. Zhuang, “An efficient spatio-temporal pyramid transformer for action detection,” in *European Conference on Computer Vision*. Springer, 2022, pp. 358–375.
- [51] X. Liu, Q. Wang, Y. Hu, X. Tang, S. Zhang, S. Bai, and X. Bai, “End-to-end temporal action detection with transformer,” *IEEE Transactions on Image Processing*, vol. 31, pp. 5427–5441, 2022.
- [52] M.-G. Gan and Y. Zhang, “Temporal attention-pyramid pooling for temporal action detection,” *IEEE Transactions on Multimedia*, 2022.
- [53] S. Nag, X. Zhu, Y. Song, and T. Xiang, “Post-processing temporal action detection,” in *Proceedings of the IEEE/CVF Conference on Computer Vision and Pattern Recognition*, 2023, pp. 18 837–18 845.
- [54] T.-K. Kang, G.-H. Lee, K.-M. Jin, and S.-W. Lee, “Action-aware masking network with group-based attention for temporal action localization,” in *Proceedings of the IEEE/CVF Winter Conference on Applications of Computer Vision*, 2023, pp. 6058–6067.
- [55] J. Kim, M. Lee, and J.-P. Heo, “Self-feedback detr for temporal action detection,” in *Proceedings of the IEEE/CVF International Conference on Computer Vision*, 2023, pp. 10 286–10 296.
- [56] Z. Zhao, D. Wang, and X. Zhao, “Movement enhancement toward multi-scale video feature representation for temporal action detection,” in *Proceedings of the IEEE/CVF International Conference on Computer Vision*, 2023, pp. 13 555–13 564.
- [57] K. Xia, L. Wang, Y. Shen, S. Zhou, G. Hua, and W. Tang, “Exploring action centers for temporal action localization,” *IEEE Transactions on Multimedia*, 2023.
- [58] J. Shao, X. Wang, R. Quan, J. Zheng, J. Yang, and Y. Yang, “Action sensitivity learning for temporal action localization,” *arXiv preprint arXiv:2305.15701*, 2023.
- [59] D. Shi, Y. Zhong, Q. Cao, L. Ma, J. Li, and D. Tao, “Tridet: Temporal action detection with relative boundary modeling,” in *Proceedings of the IEEE/CVF Conference on Computer Vision and Pattern Recognition*, 2023, pp. 18 857–18 866.
- [60] R. Zeng, W. Huang, M. Tan, Y. Rong, P. Zhao, J. Huang, and C. Gan, “Graph convolutional networks for temporal action localization,” in *Proceedings of the IEEE/CVF international conference on computer vision*, 2019, pp. 7094–7103.
- [61] H. Alwassel, S. Giancola, and B. Ghanem, “Tsp: Temporally-sensitive pretraining of video encoders for localization tasks,” in *Proceedings of the IEEE/CVF International Conference on Computer Vision*, 2021, pp. 3173–3183.